Received: 16 December 2021 | Revised: 2 July 2022 | Accepted: 21 August 2022

DOI: 10.1002/nme.7106

RESEARCH ARTICLE

WILEY

A non-conforming finite element formulation for modeling compressible viscous fluid and flexible solid interaction

Hamideh Hassanpour Guilvaiee[1] | **Florian Toth**[1] | **Manfred Kaltenbacher**[2]

[1]Institute of Mechanics and Mechatronics, TU Wien, Vienna, Austria

[2]Institute of Fundamentals and Theory in Electrical Engineering (IGTE), TU Graz, Graz, Austria

Correspondence
Hamideh Hassanpour Guilvaiee, Institute of Mechanics and Mechatronics, TU Wien, Vienna, Austria.
Email: hamideh.hassanpour@tuwien.ac.at

Funding information
Austrian Research Promotion Agency (FFG), Grant/Award Number: 868033

Abstract

In modeling fluid–solid interaction (FSI), considering the impact of fluid compressibility is necessary to describe sound propagation. Furthermore, in micro-scale, fluid viscosity is important. We present a finite element formulation for modeling a flexible solid coupled to a compressible viscous fluid. We use the linearized Navier–Stokes equations for a Newtonian fluid and describe the linear elastic solid using the linearized balance of momentum. For coupling between fluid and solid, we develop a non-conforming finite element formulation, and propose an estimation for the necessary penalty factor by applying a scaling approach. The formulation is validated based on several test cases for various material combinations and shows good agreement with analytical solutions. Further, Nitsche-based and symmetrization-free formulations are compared, and spatial convergence is studied. Finally, we present an application example of a miniature Helmholtz resonator, which depicts a notable impact of the solid interaction on the viscous flow. In sum, our study indicates the potential for widespread use of the presented numerical approach in modeling FSI in miniature systems.

KEYWORDS

compressible-viscous fluid, finite element method, non-conforming mesh

1 | INTRODUCTION

The interaction of a viscous fluid with an elastic structure has been studied in various fields, from porous media to micro-electromechanical systems applications.[1-3] In such applications, the mechanical displacement is small and the effect of the arising mechanical deformations on the flow can be neglected, and linearized partial differential equations (PDEs) are solved on the initial configuration. Furthermore, in most of these applications, the steady state solution is of interest and the coupled PDEs are solved in the frequency domain. A major challenge, however, is the different requirements for the computational meshes of the individual sub-domains of the solid and the compressible viscous fluid. The non-conforming finite element methods (FEMs), for example, Nitsche-based methods, allow the coupling of two or more sub-domains with quite different mesh sizes. In doing so, the flexibility of choosing an optimal grid for each sub-domain is obtained. In cases, where the mechanical deformations are large and have to be considered for the physical equations being solved in the fluid domain, the arbitrary Lagrangian–Eulerian (ALE) formulation for modeling fluid–solid interaction (FSI) is

often used.[4-6] The ALE method allows modeling large solid deformation and its effect on the fluid domain. This usually requires suitable mesh-moving algorithms.[7]

The Nitsche method, which was originally introduced for handling Dirichlet boundary conditions,[8] has been widely used in various fields, including heat and mass transfer, solid mechanics, fluid mechanics, acoustics, and multi-physics problems.[9-12] Regarding fluid-structure interaction, compared to most formulations involving Lagrange multipliers, the Nitsche method avoids the arising saddle point problems.[13-15] Hansbo and Hermansson[16] studied an eigenproblem for the coupling of non-viscous compressible fluid and flexible solid using the Nitsche method. Later, Hansbo et al. presented a space-time FEM applying the Nitsche method for coupling viscous incompressible fluids and linearly elastic structures.[17] Rüberg et al. used the Nitsche method combined with a stabilization technique to model the interaction between an incompressible viscous fluid and a thin structure.[18] They presented a fixed-grid finite element technique valid for curved grid lines and a nonuniform cell size. Burman et al.[19] extended the Nitsche-based method by introducing a ghost-penalty stabilization term for incompressible fluid-structure interaction. Dettmer et al.[20] applied the non-symmetric and penalty-free Nitsche method in an immersed boundary FEM. They employed the ghost-penalty terms to reduce the system matrix condition number resulting from the small cut cells. They extended their work by presenting a robust FEM to model incompressible viscous FSI, using the Nitsche method, to enforce the kinematic conditions at the interface.[7] Building on these studies, we present a novel formulation for coupling an elastic structure and a compressible, viscous fluid. Our work focuses on two main issues: first, we study the numerical penalty factor's impact at the fluid–solid interface, offering guidelines for its choice. Second, we present an application example highlighting the advantages of solid interaction on a miniature Helmholtz resonator using the non-conforming grid technique.

Viscous effects are pronounced when the thickness of the viscous boundary layer is in the same order of magnitude as characteristic problem dimensions, such as in electronic and medical devices (miniature microphones, loudspeakers, hearing aids).[21,22] Common approaches that include viscous effects to describe fluid behavior are the impedance-like boundary condition[23-25] and low reduced frequency models, in which the pressure is assumed constant over the cross-section.[26-28] Although being computationally efficient, these models have geometry restrictions. The low reduced frequency model is used for cases where the acoustic wavelength is considerably larger than the viscous boundary layer thickness and the geometry length scale. The impedance-like boundary condition is suggested for cases where the viscous boundary layer thickness is sufficiently small compared to the relevant features of the investigated geometry. On the contrary, the full linearized Navier–Stokes (FLNS) formulation fulfills the fluid-structure coupling conditions and can simulate a compressible viscous fluid. However, FLNS formulation is computationally more demanding.[26,28-30]

The current study develops a finite element formulation to model the interaction between compressible viscous fluids and solids. For the fluid, we use FLNS, and for the solid, we use the balance of momentum for linear elastic solid. We then implemented and solved our model in the open-source program openCFS.[31] We further propose a formulation for choosing a suitable value of the penalty factor. Later, we verify our model with multiple examples that consider various combinations of materials. Finally, as an application example, we use our method to design a 2-dimensional (2D) miniature Helmholtz resonator with a flexible end-plate and further study the impact of FSI on the Helmholtz resonator characteristics.

2 | PROBLEM FORMULATION

We consider an elastic solid coupled to a viscous, compressible fluid along with a common interface. Figure 1 shows a typical fluid-structure interaction geometry with an elastic solid region Ω_s, a compressible viscous fluid Ω_f, the common interface Γ_{sf} between both regions and the boundaries Γ_t, Γ_0, Γ_r, and Γ_s where suitable boundary conditions have to be applied. The behavior of the solid is described by the balance of momentum and a suitable constitutive law (Hooke's law). The governing equations in the fluid domain Ω_f are the balance of mass and momentum as well as an equation of state and constitutive law (Newtonian fluid).

To linearize the non-linear governing equations of the fluid, we apply the perturbation ansatz for the unknowns density, pressure, and velocity

$$\bar{\rho}(\boldsymbol{x},t) = \rho_f(\boldsymbol{x}) + \rho(\boldsymbol{x},t) \qquad \bar{p}(\boldsymbol{x},t) = p_f(\boldsymbol{x}) + p(\boldsymbol{x},t) \qquad \bar{\boldsymbol{v}}(\boldsymbol{x},t) = \boldsymbol{v}_f(\boldsymbol{x}) + \boldsymbol{v}(\boldsymbol{x},t), \tag{1}$$

where the bar $\bar{(.)}$ denotes the total quantity, which is split into a temporally constant background quantity denoted by index $(.)_f$, and the perturbation quantity, which is assumed to be small. For simplicity, we assume that there is no background

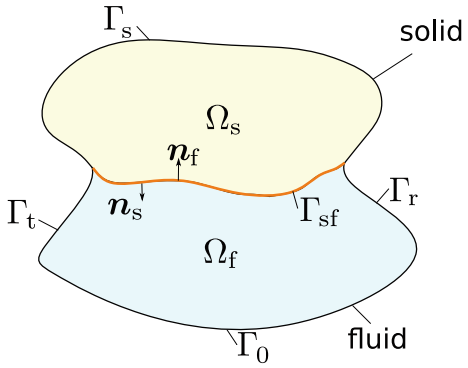

FIGURE 1 Simple sketch of a solid–fluid interaction problem including elastic solid Ω_s and viscous fluid Ω_f domains with their interface Γ_{sf} . The outer normal vector of the solid and fluid domains are $\boldsymbol{n}_s$ and $\boldsymbol{n}_f$, respectively.

velocity ($\boldsymbol{v}_f = 0$). To obtain the linearized balance of mass and momentum, we first insert the perturbation ansatz (1) into the balance of mass and momentum. Then by excluding the non-linear terms and using the linearized equation of state $\rho = \frac{p}{c^2}$ (c donates the speed of sound), and only retaining linear terms of the remaining solution variables (pressure p and velocity $\boldsymbol{v}$), one obtains the linearized balance of mass and momentum

$$\frac{1}{c^2}\frac{\partial p}{\partial t} + \boldsymbol{\nabla}\cdot(\rho_f \boldsymbol{v}) = 0 \quad \text{in } \Omega_f, \tag{2}$$

$$\rho_f \frac{\partial \boldsymbol{v}}{\partial t} - \boldsymbol{\nabla}\cdot\boldsymbol{\sigma}_f = \boldsymbol{f}_f \quad \text{in } \Omega_f. \tag{3}$$

The adiabatic speed of sound $c = \sqrt{K_f/\rho_f}$ is computed from the adiabatic bulk modulus K_f and the background fluid density ρ_f. The operators $\boldsymbol{\nabla}$ and $\boldsymbol{\nabla}\cdot$ are the gradient and the divergence operators, respectively, and t denotes the time. The external volume force density acting in the fluid domain is $\boldsymbol{f}_f$. The fluid stress tensor $\boldsymbol{\sigma}_f$ for an isotropic Newtonian fluid is written as

$$\begin{aligned}\boldsymbol{\sigma}_f &= -p\boldsymbol{I} + \boldsymbol{\tau} \\ &= -p\boldsymbol{I} + \mu\left(\boldsymbol{\nabla}\boldsymbol{v} + (\boldsymbol{\nabla}\boldsymbol{v})^T\right) + \left(\mu_b - \frac{2}{3}\mu\right)(\boldsymbol{\nabla}\cdot\boldsymbol{v})\boldsymbol{I},\end{aligned} \tag{4}$$

where $\boldsymbol{\tau}$ is the viscous stress tensor, μ the dynamic (or shear) viscosity and μ_b the bulk (or volume) viscosity.

The elastic solid in Ω_s is governed by the conservation of momentum

$$\rho_s \frac{\partial^2 \boldsymbol{u}}{\partial t^2} - \boldsymbol{\nabla}\cdot\boldsymbol{\sigma}_s = \boldsymbol{f}_s \quad \text{in } \Omega_s, \tag{5}$$

where the solid density is denoted by ρ_s, $\boldsymbol{u}$ is the displacement vector, $\boldsymbol{\sigma}_s$ is the mechanical stress tensor, and $\boldsymbol{f}_s$ is the external force per unit volume acting in the solid domain. For linear elastic material behavior, $\boldsymbol{\sigma}_s$ may be written as

$$\boldsymbol{\sigma}_s = \boldsymbol{C} : \boldsymbol{\epsilon}, \tag{6}$$

where : denotes the double contraction between the stiffness tensor $\boldsymbol{C}$ and the strain tensor $\boldsymbol{\epsilon}$. Assuming small displacements, we can compute the strain tensor by

$$\boldsymbol{\epsilon} = \frac{1}{2}\left(\boldsymbol{\nabla}\boldsymbol{u} + (\boldsymbol{\nabla}\boldsymbol{u})^T\right). \tag{7}$$

Finally, we need to apply boundary and coupling conditions. On the wall boundary of solid Γ_s and fluid Γ_0, we enforce zero displacements and velocity vector, respectively. On the symmetry boundaries, their vector components perpendicular

to the boundaries are zero. At the interface Γ_{sf} between solid and fluid, one needs to enforce the dynamic and kinematic conditions requiring continuity of traction and velocity, respectively. Traction continuity is enforced by requiring

$$\boldsymbol{\sigma}_s \cdot \boldsymbol{n}_s = -\boldsymbol{\sigma}_f \cdot \boldsymbol{n}_f \quad \text{on } \Gamma_{sf}, \tag{8}$$

where $\boldsymbol{n}_f$ and $\boldsymbol{n}_s$ are normal vectors of the interface pointing out of the fluid and solid domain, respectively (see Figure 1). The second interface condition is velocity continuity at the interface, which requires

$$\frac{\partial \boldsymbol{u}}{\partial t} = \boldsymbol{v} \quad \text{on } \Gamma_{sf}. \tag{9}$$

3 | FINITE ELEMENT FORMULATION

To obtain the weak form of the formulation needed for the finite element solution of FSI, we multiply the strong forms by appropriate test functions and integrate them over the whole computational domain. The conservation of mass in its weak form is derived from Equation (2) and reads

$$\int_{\Omega_f} p' \rho_f \nabla \cdot \boldsymbol{v} \, d\Omega + \int_{\Omega_f} p' \frac{1}{c^2} \frac{\partial p}{\partial t} \, d\Omega = 0. \tag{10}$$

The weak form of conservation of momentum for fluid and solid are derived from Equations (3) and (5) by applying the Green's theorem

$$\int_{\Omega_f} \rho_f \boldsymbol{v}' \cdot \frac{\partial \boldsymbol{v}}{\partial t} \, d\Omega + \int_{\Omega_f} \nabla \boldsymbol{v}' : \boldsymbol{\sigma}_f \, d\Omega - \int_{\Gamma_f} (\boldsymbol{v}' \cdot \boldsymbol{\sigma}_f) \cdot \boldsymbol{n}_f \, d\Gamma = \boldsymbol{0}, \tag{11}$$

$$\int_{\Omega_s} \rho_s \boldsymbol{u}' \cdot \frac{\partial^2 \boldsymbol{u}}{\partial t^2} \, d\Omega + \int_{\Omega_s} \nabla \boldsymbol{u}' : \boldsymbol{\sigma}_s \, d\Omega - \int_{\Gamma_s} (\boldsymbol{u}' \cdot \boldsymbol{\sigma}_s) \cdot \boldsymbol{n}_s \, d\Gamma = \boldsymbol{0}. \tag{12}$$

In these equations, $\boldsymbol{v}'$, $\boldsymbol{u}'$, and p' are fluid velocity test function, mechanical displacement test function, and pressure test function, respectively. The normal vector $\boldsymbol{n}_i$ of the boundary Γ_i points out of the domain Ω_i (i is f and s for the fluid and solid, respectively). Note that, for the sake of simplicity the external forces for both domains have been set to zero ($\boldsymbol{f}_f = \boldsymbol{f}_s = \boldsymbol{0}$). In the fluid domain, we use the inf-sup condition, also known as the Ladyzhenskaya–Babuska–Brezzi (LBB) condition, to obtain well-posedness, ensuring that the elements do not lock and the pressure does converge. To meet the inf-sup condition, we use a one-order higher polynomial basis function for velocity than that for the pressure.[32,33]

For modeling fluid-structure interaction, we adapt the Nitsche method because it offers multiple advantages. First, it does not introduce any other unknowns at the interface, such as those used in most of the Lagrange multiplier-based methods. Thus, it prevents saddle point problems in the discretized system. Second, since this method applies the coupling conditions in a weak sense, it can be used on non-conforming meshes, which are convenient for mesh generation. To obtain the coupling formulation, we combine (11) and (12). Then we apply the traction continuity condition (8) to ensure traction continuity at the interface *(term traction consistency)* and add the penalty term *(term penalty)* to guarantee the continuity of velocities. We keep the solid stress tensor for the simpler implementation since it contains only the displacement as an unknown

$$\begin{aligned} &\int_{\Omega_f} \rho_f \boldsymbol{v}' \cdot \frac{\partial \boldsymbol{v}}{\partial t} \, d\Omega + \int_{\Omega_f} \nabla \boldsymbol{v}' : \boldsymbol{\sigma}_f \, d\Omega + \int_{\Omega_s} \rho_s \boldsymbol{u}' \cdot \frac{\partial^2 \boldsymbol{u}}{\partial t^2} \, d\Omega + \int_{\Omega_s} \nabla \boldsymbol{u}' : \boldsymbol{\sigma}_s \, d\Omega \\ &\underbrace{- \int_{\Gamma_{sf}} (\boldsymbol{u}' - \boldsymbol{v}') \cdot \boldsymbol{\sigma}_s \cdot \boldsymbol{n} \, d\Gamma}_{\text{traction consistency}} \underbrace{+ \beta \frac{p_e^2}{h_e} \int_{\Gamma_{sf}} (\boldsymbol{u}' - \boldsymbol{v}') \cdot \left(\frac{\partial \boldsymbol{u}}{\partial t} - \boldsymbol{v} \right) d\Gamma}_{\text{penalty}} + \underbrace{\int_{\Gamma_{sf}} \boldsymbol{\sigma}_s(\boldsymbol{u}') \left(\boldsymbol{v} - \frac{\partial \boldsymbol{u}}{\partial t} \right) \cdot \boldsymbol{n} \, d\Gamma}_{\text{symmetrization term}} = \boldsymbol{0}. \end{aligned} \tag{13}$$

In Nitsche-base formulation, the *symmetrization* term (last term in (13)) is added. However, it has to be noted that the describing equations (see Section 2) are non-symmetric; thus, the overall formulations stay non-symmetric. Hereafter, in this work, the formulations with and without the symmetrization term are called the Nitsche-based and the symmetrization-free formulations, respectively, and results of these two formulations (with and without the symmetrization term) are compared.

The penalty term in (13) contains the element order $p_e = \max(p_s, p_f)$ to account various polynomial orders, where, p_s and p_f are the order of basic functions for solid and fluid domains, respectively. Furthermore, we add $1/h_e$ to the penalty term, where $h_e = \min(h_f, h_s)$ that is, the smallest element length of fluid or solid elements on the non-conforming interface. This guarantees that the resulting system is positive definite.[34] The normal direction of the interface $\boldsymbol{n}$ is defined that is, as $\boldsymbol{n} = \boldsymbol{n}_s = -\boldsymbol{n}_f$. The basis of our implementation in the open source finite element framework openCFS[31] for modeling fluid-structure interaction contains the balance of the mass (10) and the conservation of momentum for solid and fluid including the coupling term (13). The final equations can be summarized by inserting $\boldsymbol{\sigma}_f$ and $\boldsymbol{\sigma}_s$ as the following

$$\int_{\Omega_f} p' \rho_f \boldsymbol{\nabla} \cdot \boldsymbol{v} \, \mathrm{d}\Omega + \int_{\Omega_f} p' \frac{1}{c^2} \frac{\partial p}{\partial t} \, \mathrm{d}\Omega = 0, \tag{14a}$$

$$\begin{aligned} &\int_{\Omega_f} \rho_f \boldsymbol{v}' \cdot \frac{\partial \boldsymbol{v}}{\partial t} \, \mathrm{d}\Omega - \int_{\Omega_f} \boldsymbol{\nabla} \boldsymbol{v}' : p\boldsymbol{I} \, \mathrm{d}\Omega + \int_{\Omega_f} \mu \boldsymbol{\nabla} \boldsymbol{v}' : \left(\boldsymbol{\nabla} \boldsymbol{v} + (\boldsymbol{\nabla} \boldsymbol{v})^T \right) \mathrm{d}\Omega + \int_{\Omega_f} (\mu_b - \frac{2}{3}\mu) \boldsymbol{\nabla} \boldsymbol{v}' : (\boldsymbol{\nabla} \cdot \boldsymbol{v}) \boldsymbol{I} \, \mathrm{d}\Omega \\ &+ \int_{\Gamma_{sf}} \boldsymbol{v}' \cdot \boldsymbol{C} : \frac{1}{2} \left(\boldsymbol{\nabla} \boldsymbol{u} + (\boldsymbol{\nabla} \boldsymbol{u})^T \right) \cdot \boldsymbol{n} \, \mathrm{d}\Gamma - \beta \frac{p_e^2}{h_e} \int_{\Gamma_{sf}} \boldsymbol{v}' \cdot \frac{\partial \boldsymbol{u}}{\partial t} \, \mathrm{d}\Gamma + \beta \frac{p_e^2}{h_e} \int_{\Gamma_{sf}} \boldsymbol{v}' \cdot \boldsymbol{v} \, \mathrm{d}\Gamma = \boldsymbol{0}, \end{aligned} \tag{14b}$$

$$\begin{aligned} &\int_{\Omega_s} \rho_s \boldsymbol{u}' \cdot \frac{\partial^2 \boldsymbol{u}}{\partial t^2} \, \mathrm{d}\Omega + \int_{\Omega_s} \boldsymbol{\nabla} \boldsymbol{u}' : \boldsymbol{C} : \frac{1}{2} \left(\boldsymbol{\nabla} \boldsymbol{u} + (\boldsymbol{\nabla} \boldsymbol{u})^T \right) \mathrm{d}\Omega \\ &- \int_{\Gamma_{sf}} \boldsymbol{u}' \cdot \boldsymbol{C} : \frac{1}{2} \left(\boldsymbol{\nabla} \boldsymbol{u} + (\boldsymbol{\nabla} \boldsymbol{u})^T \right) \cdot \boldsymbol{n} \, \mathrm{d}\Gamma + \beta \frac{p_e^2}{h_e} \int_{\Gamma_{sf}} \boldsymbol{u}' \cdot \frac{\partial \boldsymbol{u}}{\partial t} \, \mathrm{d}\Gamma - \beta \frac{p_e^2}{h_e} \int_{\Gamma_{sf}} \boldsymbol{u}' \cdot \boldsymbol{v} \, \mathrm{d}\Gamma \\ &\underbrace{+ \int_{\Gamma_{sf}} \frac{1}{2} \boldsymbol{C} : \nabla \boldsymbol{u}' \boldsymbol{v} \cdot \boldsymbol{n} \, \mathrm{d}\Gamma - \int_{\Gamma_{sf}} \frac{1}{2} \boldsymbol{C} : \nabla \boldsymbol{u}' \frac{\partial \boldsymbol{u}}{\partial t} \cdot \boldsymbol{n} \, \mathrm{d}\Gamma + \int_{\Gamma_{sf}} \frac{1}{2} \boldsymbol{C} : (\nabla \boldsymbol{u}')^T \boldsymbol{v} \cdot \boldsymbol{n} \, \mathrm{d}\Gamma - \int_{\Gamma_{sf}} \frac{1}{2} \boldsymbol{C} : (\nabla \boldsymbol{u}')^T \frac{\partial \boldsymbol{u}}{\partial t} \cdot \boldsymbol{n} \, \mathrm{d}\Gamma}_{\text{symmetrization term}} = \boldsymbol{0}. \end{aligned} \tag{14c}$$

As mentioned in the introduction, in many applications, the steady state solution to harmonic forcing is of interest, and the coupled PDEs are solved in the frequency domain. Harmonic forcing in any quantity f with angular frequency ω can be represented by $f = \Re\{\hat{f} e^{i\omega t}\}$, with $i = \sqrt{-1}$ and $\hat{f} \in \mathbb{C}$. To obtain the harmonic FEM formulation, we perform a Fourier transform of (14a)–(14c) and apply the standard continuous Galerkin FEM[35] in which we approximate the continuous pressure p, fluid velocity $\boldsymbol{v}$, and the mechanical displacement $\boldsymbol{u}$ via

$$p \approx p_h = \sum_{i=1}^{n_{eq}^p} N_i^p p_i, \tag{15}$$

$$\boldsymbol{v} \approx \boldsymbol{v}_h = \sum_{i=1}^{n_{eq}^v} \sum_{j=1}^{n_d} N_i^v v_{ij} \boldsymbol{e}_j = \sum_{i=1}^{n_{eq}^v} \boldsymbol{N}_i^v \boldsymbol{v}_i \;\; ; \;\; \boldsymbol{N}_i^v = \begin{pmatrix} N_i^v & 0 & 0 \\ 0 & N_i^v & 0 \\ 0 & 0 & N_i^v \end{pmatrix}, \tag{16}$$

$$\boldsymbol{u} \approx \boldsymbol{u}_h = \sum_{i=1}^{n_{eq}^u} \sum_{j=1}^{n_d} N_i^u u_{ij} \boldsymbol{e}_j = \sum_{i=1}^{n_{eq}^u} \boldsymbol{N}_i^u \boldsymbol{u}_i \;\; ; \;\; \boldsymbol{N}_i^u = \begin{pmatrix} N_i^u & 0 & 0 \\ 0 & N_i^u & 0 \\ 0 & 0 & N_i^u \end{pmatrix}. \tag{17}$$

In (15)–(17) n_{eq}^p, n_{eq}^v, n_{eq}^u denotes the number of equations for the pressure, velocity, displacement, respectively, and n_d is the number of space dimension. Furthermore, N_i^p, N_i^v, N_i^u are the appropriate basis functions and $\boldsymbol{e}_j$ is the space unit

vector for the j direction. Substituting (15)–(17) into the Fourier transformed weak formulation results in the following system of equations

$$\left[\begin{pmatrix}0&0&0\\0&0&0\\0&0&\boldsymbol{M_{uu}}\end{pmatrix}-\omega^2+i\omega\begin{pmatrix}\boldsymbol{C_{pp}}&0&0\\0&\boldsymbol{C_{vv}}&\boldsymbol{C_{vu}}\\0&0&\boldsymbol{C_{uu}}\end{pmatrix}+\begin{pmatrix}0&\boldsymbol{K_{pv}}&0\\\boldsymbol{K_{vp}}&\boldsymbol{K_{vv}}&\boldsymbol{K_{vu}}\\0&\boldsymbol{K_{uv}}&\boldsymbol{K_{uu}}\end{pmatrix}\right]\begin{pmatrix}\{p\}\\\{\boldsymbol{v}\}\\\{\boldsymbol{u}\}\end{pmatrix}=\begin{pmatrix}\boldsymbol{S_{pp}}&\boldsymbol{S_{pv}}&0\\\boldsymbol{S_{vp}}&\boldsymbol{S_{vv}}&\boldsymbol{S_{vu}}\\0&\boldsymbol{S_{uv}}&\boldsymbol{S_{uu}}\end{pmatrix}\begin{pmatrix}\{p\}\\\{\boldsymbol{v}\}\\\{\boldsymbol{u}\}\end{pmatrix}=\begin{pmatrix}\{0\}\\\{f_{\boldsymbol{v}}\}\\\{f_{\boldsymbol{u}}\}\end{pmatrix}. \tag{18}$$

In (18) $\boldsymbol{M}_{ij}$, $\boldsymbol{C}_{ij}$, and $\boldsymbol{K}_{ij}$ refer to the non-zero sub-blocks of mass, damping and stiffness matrices, respectively. Combined, they form the complex valued system matrix of the harmonic problem. Here, $\boldsymbol{S}_{pp}$ and $\boldsymbol{S}_{p\boldsymbol{v}}$ contain the bi-linear terms in balance of mass (14a), $\boldsymbol{S}_{\boldsymbol{v}p}$, $S_{\boldsymbol{vu}}$, and $\boldsymbol{S}_{\boldsymbol{vv}}$ contain the bi-linear terms in fluid balance of momentum (14b) and, $\boldsymbol{S}_{\boldsymbol{uu}}$, $\boldsymbol{S}_{\boldsymbol{uv}}$ contain the bi-linear terms in solid balance of momentum (14c) with their surface coupling terms. Moreover, $\{p\}$, $\{\boldsymbol{v}\}$, $\{\boldsymbol{u}\}$ are the unknown vectors of the pressure, velocity, and displacement, respectively. On the right side of the equation (18), $\{f_{\boldsymbol{v}}\}$ and $\{f_{\boldsymbol{u}}\}$ represent the inhomogeneous Neumann boundary conditions or non-zero volume forces.

The evaluation of the coupling integrals (traction consistency and penalty terms) is not straightforward since some of the arising bi-linear forms are made up of the ansatz and test functions defined on different (non-conforming) grids. We compute an intersection mesh between the two grids and use this intersection mesh for the integration. The contributions to the system matrices are then obtained by evaluating the ansatz functions of both original grids at the locations of the integration points of the intersection mesh.[35,36]

The intersection mesh at the interface contains vertexes of both master and slave meshes. The generation of the intersection mesh for straight interfaces in 2D is not complicated. However, the intersection of curved interfaces in 2D and especially 3D is more complex since the interface elements have to be mapped to a common curve or surface before the actual intersection operations. One possible approach[37] relies on pair-wise projections of the elements to the slave elements at the interface along the face normal vector. For slightly mismatching meshes, this method leads to high aspect-ratio elements and consequently poor results due to inaccuracies in the numerical integration.[35,38] To avoid high aspect-ratio elements, one may discard them as is done in our implementation or apply spline-based finite elements.[39]

Finally, the penalty factor β is considered to make the formulation dimensionally consistent and to enforce the velocity continuity. Determining a suitable penalty factor is crucial in solving the formulation: a small value of the penalty factor does not meet velocity continuity at the interface. In contrast, a high value of the penalty factor results in a high condition number of the arising system matrix. To obtain the suitable penalty factor, we study the system of linear equations and set the penalty terms to have a value in the scale of the surrendering terms. To do so, we compute how the values of each term in the system matrix are scaled and then calculate an estimation for the penalty factor.

We consider that the volume and surface integrals are in the scale of h^3 and h^2, respectively, and the space derivative, as well as the strain, are in the scale of $\frac{1}{h}$. The element size h is h_{s} in solid and h_{f} in fluid. Furthermore, the first and second-time derivatives are scaling in the frequency domain by $i\omega$ and $-\omega^2$, respectively. Writing the scaling value for example, for $(-\omega^2)\int_{\Omega_{\mathrm{s}}}\rho_{\mathrm{s}}(\boldsymbol{N}_i^u)^T(\boldsymbol{N}_j^u)\,\mathrm{d}\Omega$, which contributes in $S_{\boldsymbol{uu}}$, gives us the scale of $(\rho_{\mathrm{s}})(-\omega^2)(h_{\mathrm{s}}^3)$. Applying this procedure to the other terms in the formulation with non-symmetrization terms reveals that the entries in $S_{\boldsymbol{uu}}$ and in $S_{\boldsymbol{vu}}$ (except the penalty terms) scale with Eh_{s}. The entries in $S_{\boldsymbol{vv}}$ scale with either $\rho_{\mathrm{f}}(i\omega)(h_{\mathrm{f}}^3)$ or μh_{f}. Nonetheless, applying the solid and fluid element size rules indicate that all existing terms in $\boldsymbol{S}_{\boldsymbol{uu}}$ and $\boldsymbol{S}_{\boldsymbol{vv}}$ have the scale of Eh_{s} and μh_{f}, respectively. The solid element size should be chosen based on the wavelength $\lambda_{\mathrm{s}} = \frac{c_{\mathrm{s}}}{f}$, thus

$$h_{\mathrm{s}} \sim \frac{c_{\mathrm{s}}}{\omega} \sim \frac{1}{\omega}\sqrt{\frac{E}{\rho_{\mathrm{s}}}}, \tag{19}$$

where c_{s} is the speed of sound in the solid. In viscous fluid, the fluid element size is in the order of the viscous boundary layer

$$h_{\mathrm{f}} \sim \sqrt{\frac{\mu}{\rho_{\mathrm{f}}\omega}}. \tag{20}$$

One can obtain Eh_{s} and μh_{f} by inserting (19) into $\rho_{\mathrm{s}}\omega^2 h_{\mathrm{s}}^3$ and (20) into $\rho_{\mathrm{f}}\omega h_{\mathrm{f}}^3$, respectively.

Since all the terms in $\boldsymbol{S_{uu}}$ and $\boldsymbol{S_{vu}}$ are proportional to Eh_s, a scale for the penalty factor β can be proposed. Thus we write

$$Eh_s \sim \beta \frac{p_e^2}{h_e}(\omega)(h_s^2),$$
$$\beta \sim \frac{E}{h_s \omega}\frac{h_e}{p_e^2}. \tag{21}$$

Similarly, the terms in $\boldsymbol{S_{vv}}$ propose that the penalty factor scales with

$$\mu h_f \sim \beta \frac{p_e^2}{h_e} h_f^2,$$
$$\beta \sim \frac{\mu}{h_f}\frac{h_e}{p_e^2}. \tag{22}$$

In this formulation, the term $\boldsymbol{S_{uv}}$ only contains the penalty factor; therefore, no comparison can be made here. In the Nitsche-based formulation the entries in $\boldsymbol{S_{uu}}$ gives an additional scale of $E\omega h_s$. Therefore, one has

$$Eh_s\omega \sim \beta \frac{p_e^2}{h_e}(\omega)(h_s^2),$$
$$\beta \sim \frac{E}{h_s}\frac{h_e}{p_e^2}. \tag{23}$$

In addition, in this formulation the term $\boldsymbol{S_{uv}}$ is also scaled with Eh_s . From scaling we retained two relations (21) and (22) for the penalty factor. These relations prove that the formulation is physically consistent by considering viscosity (μ) or Young's modulus over angular velocity $\left(\frac{E}{\omega}\right)$ in the penalty factor. We consider the summation of these relations as the scaling penalty factor. For the symmetrization-free formulation the scaling factor is

$$\beta_{\text{scaling},s} = \left(\frac{E}{h_s\omega} + \frac{\mu}{h_f}\right)\frac{h_e}{p_e^2}, \tag{24}$$

whereas for Nitsche-based formulation it is defined as

$$\beta_{\text{scaling},n} = \left(\frac{E}{h_s\omega} + \frac{\mu}{h_f} + \frac{E}{h_s}\right)\frac{h_e}{p_e^2}. \tag{25}$$

This formulation suggests that the scaling penalty factor depends on both physical quantities (e.g., viscosity and Young's modulus) and the meshing parameters (e.g., the fluid and solid element mesh size). Note that this scaling term ensures that the bi-linear forms, including the penalty factor, are in the order of the other bi-linear terms. However, to enforce these bi-linear terms or, explicitly, the continuity of velocity at the interface, we propose to scale them by including the user-defined numerical penalty factor β_{numeric}

$$\beta = \beta_{\text{scaling},i}\beta_{\text{numeric}} \quad i \in \{s, n\}. \tag{26}$$

In the following sections, we investigate the suitable range of β_{numeric} in the symmetrization-free and Nitsche-based formulations.

4 | NUMERICAL EXPERIMENTS

To verify our proposed formulation, we first present three case studies. In each example, we investigate the effect of the penalty factor on the field results as well as on the velocity continuity at the interface by evaluating a relative error norm (E). This error is defined as

$$E = \frac{\|\boldsymbol{u}_n - \boldsymbol{u}_a\|_2}{\|\boldsymbol{u}_a\|_2}, \tag{27}$$

where $\boldsymbol{u}_a$ and $\boldsymbol{u}_n$ are analytic and numerical results (at the considered degrees of freedom (DOF)), respectively, and $\| \dots \|_2$ denotes the Euclidean norm. Then, various material combinations were considered to examine the robustness

of our formulation. Finally, by employing this method, a miniature Helmholtz resonator with flexible end-plate is designed.

All results were obtained using our open source FEM program openCFS.[31] In all the numerical studies, basis functions of second order were used for velocity and displacement, and basis functions of first order were used for pressure DOF. The resulting linear system of equations was solved by the PARDISO solver[40] included in Intel's MKL[41] which is sufficiently robust to deal with badly conditioned system matrices.

4.1 | One-dimensional wave propagation

Our first example illustrates one-dimensional (1D) wave propagation of a compressible viscous fluid coupled to an elastic solid. A comparison is then made with an analytical solution (derivation of the analytical solution is described in Appendix A). In this example, the solid material is characterized by the density $\rho_s = 1.5\ \mathrm{kg/m^3}$, the Young modulus $E = 1.0 \cdot 10^5$ Pa and the Poisson ratio $\nu = 0.4$ to obtain the compatible wavelength with the fluid (air). The air properties are described in Table 1. The sketch depicted in Figure 2 provides detailed information about the boundary conditions used in this example. The geometry dimensions are $L_1 = 0.15$ m, $L_2 = 0.20$ m and the height of the channel is 0.01 m. The study is performed at a frequency of 10 kHz and the displacement, velocity, and pressure have 4000, 40,000 and 16,000 DOF, respectively.

To determine a suitable range of numerical penalty factors, we test 16 numerical penalty factors ranging from $5 \cdot 10^{-2}$ to $5 \cdot 10^{13}$, in symmetrization-free formulation, and compare the computed velocity values with the analytical solution. Figure 3A shows velocity error versus the numerical penalty factor. The error decreases from $\sim 10^{-3}$ to a minimum of $\sim 10^{-7}$ by increasing the numerical penalty factor from $5 \cdot 10^{-2}$ to $5 \cdot 10^2$ and remains constant for the numerical penalty factor between $5 \cdot 10^2$ and $5 \cdot 10^9$. The numerical penalty factor results in an increase for the velocity error from $\sim 10^{-7}$ to $\sim 10^{-3}$ with increasing it to $5 \cdot 10^{13}$. Thus the suitable numerical penalty factor is between $5 \cdot 10^2 - 5 \cdot 10^9$. The black dashed line marked in this figure (Figure 3A) indicates the error for the $\beta_{\mathrm{numeric}} = 1$ ($\beta = \beta_{\mathrm{scaling,n}}$). Without considering this numerical penalty factor, the system does not create its lowest error showing the importance of including β_{numeric} (24).

In the Nitsche-based formulation, the velocity error is studied for various numerical penalty factors using the scaling approach (25). Figure 3B shows that the numerical penalty factors lower than 10^{10} create the minimum error of $\sim 10^{-7}$. Surprisingly, the errors remain low for very low values of the penalty factor and rapidly increase to 10. In contrast to the symmetrization-free formulation, considering $\beta_{\mathrm{numeric}} = 1$ creates the lowest error.

TABLE 1 The properties of solids and fluids

	Symbol	Air	Water
Density in $\mathrm{kg/m^3}$	ρ_f	1.225	1000
Compression modulus in Pa	K	$1.4261 \cdot 10^5$	$2.2201 \cdot 10^9$
Bulk viscosity in Pa s	μ_b	$1.22 \cdot 10^{-5}$	$3.006 \cdot 10^{-3}$
Shear viscosity in Pa s	μ	$1.829 \cdot 10^{-5}$	$1.002 \cdot 10^{-3}$

	Symbol	Steel	Nylon	Rubber	Foam
Density in $\mathrm{kg/m^3}$	ρ_s	7923.8	1100	920	1130
Poisson ratio	ν	0.3	0.4	0.49	0.49
Young modulus in GPa	E	206.8	2.1	$1.0 \cdot 10^{-4}$	$70.0 \cdot 10^{-3}$

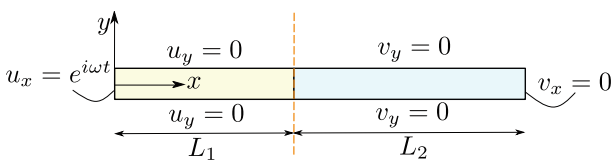

FIGURE 2 Boundary conditions for 1D wave propagation example. Yellow and blue colors show the solid and fluid regions, respectively.

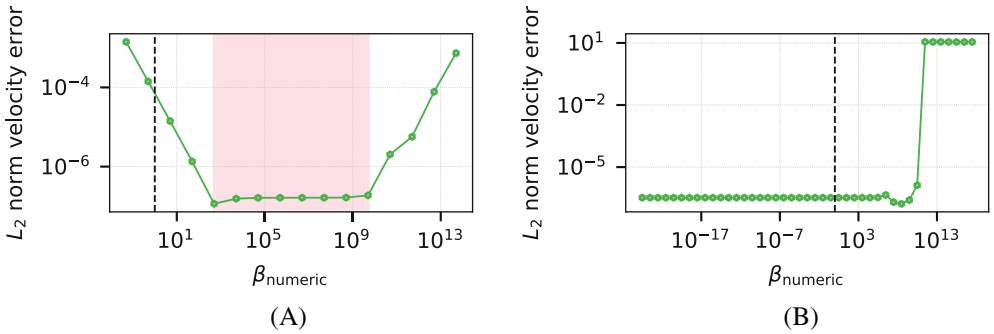

FIGURE 3 L_2 relative error norm (E) in the velocity versus numerical penalty factor for 1D wave propagation using symmetrization-free and Nitsche-based formulations. Dashed line (- - -) shows $\beta = \beta_{\text{scaling}}$ ($\beta_{\text{numeric}} = 1$). (A) Symmetrization-free formulation: Pink region depicts the suitable range of numerical penalty factors with the lowest error in the velocity; (B) Nitsche-based formulation

To illustrate how the changes in the numerical penalty factor are reflected in velocity field results, we further examine the differences created by numerical penalty factors at low ($5 \cdot 10^{-2}$), suitable ($5 \cdot 10^{5}$), and high ($5 \cdot 10^{13}$) levels. Figure 4 shows the fluid and solid real velocity field for these values of the numerical penalty factor. Using a low ($5 \cdot 10^{-2}$) value does not satisfy the velocity continuity at the interface leading to a velocity amplitude of 9.30 m/s in the solid domain versus −108.6 m/s in the fluid domain. Furthermore, the fluid velocity amplitudes are ∼5 times greater than those obtained by the analytical solution. In contrast, the velocity field results using a suitable numerical penalty factor agree with those obtained from the analytical solution with the precision of $\sim 10^{-7}$, and the continuity of velocity at the interface is met (Figure 4). This figure also shows that our formulation successfully simulates the standing wave behavior expected in the solid region and the wave attenuation caused by the viscosity effects in the fluid region with a suitable numerical penalty factor. For the high value of the numerical penalty factor ($5 \cdot 10^{13}$), however, the amplitudes of velocity at the interface are 130.3 times greater than the analytical velocity amplitudes, but the continuity of velocity is still fulfilled (Figure 4). Figure 5A shows velocity jump $\left|\boldsymbol{v} - \frac{\partial \boldsymbol{u}}{\partial t}\right|$ of 10^{-13} m/s at the interface for the high value of numerical penalty factor is lower than that for the suitable numerical penalty factor 10^{-5}. In fact, there is an inverse relationship between the numerical penalty factor and the magnitude of velocity jump at the interface (Figure 5A). Higher numerical penalty factor causes lower velocity jump since the numerical penalty factor is directly applied to the penalty term (13) that includes the velocity jump. By setting numerical the penalty factor to $5 \cdot 10^{13}$, the velocity jump at the interface decreases from $\sim 10^{2}$ to $\sim 10^{-13}$ m/s. Despite the low velocity jump at the interface, numerical penalty factors larger than $5 \cdot 10^{9}$ create large errors in the velocity field (Figure 3A) due to high condition number of the system matrix. Figure 5B shows that increasing the numerical penalty factor leads to a higher condition number of the system matrix. In the current example, for the numerical penalty factors being lower than 10^{3}, the condition number is $2 \cdot 10^{16}$. For a numerical penalty factor of 10^{14}, this value increases to $1.5 \cdot 10^{27}$. Focusing on the relative error norm, a suitable value for the numerical penalty factor in this example is between $5 \cdot 10^{2}$ and $5 \cdot 10^{9}$. The corresponding condition number on the upper bound (penalty factor of $5 \cdot 10^{9}$) is $1 \cdot 10^{23}$. The choice of the unit system impacts the conditioning of the system matrix, since the DOF (velocity, pressure, and displacement) do not share the same physical dimension. We have chosen SI units for consistency, which may be the cause of the high value of the condition number. In the following section, we provide various examples of the optimization of the numerical penalty factor using combinations of various materials.

4.2 | Rotating disc and cylindrical wave propagation

Given the different roles that bulk and shear viscosity play in fluid and FSI,[25,42] we investigate our proposed symmetrization-free formulation in two test cases that highlight the impact of each viscosity. For the sake of simplicity, we use a 2D model. The geometry is schematically depicted in Figure 6A. Boundary conditions were chosen such that either shear waves (*rotating disc*) or compression waves (*cylindrical wave*) are generated. For each case, we consider five material combinations using a non-conforming mesh at the curved fluid–solid interface.

Our first case is a rotating disc example where the shear viscosity effects were expected to be pronounced due to the shear wave propagation. To rotate the disc, we applied the harmonic tangential velocity of $v_x = -y$ m/s and $v_y = x$ m/s at

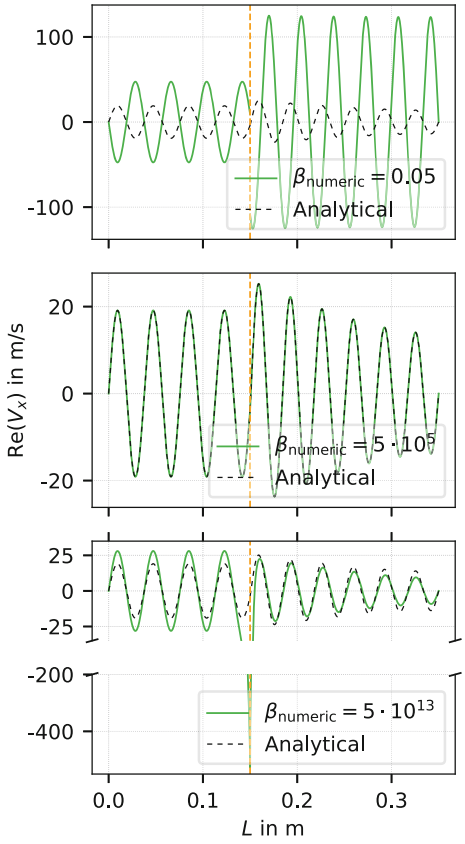

FIGURE 4 Analytical and numerical velocity field for low $(5 \cdot 10^{-2})$, suitable $(5 \cdot 10^{5})$, and high $(5 \cdot 10^{13})$ numerical penalty factor.

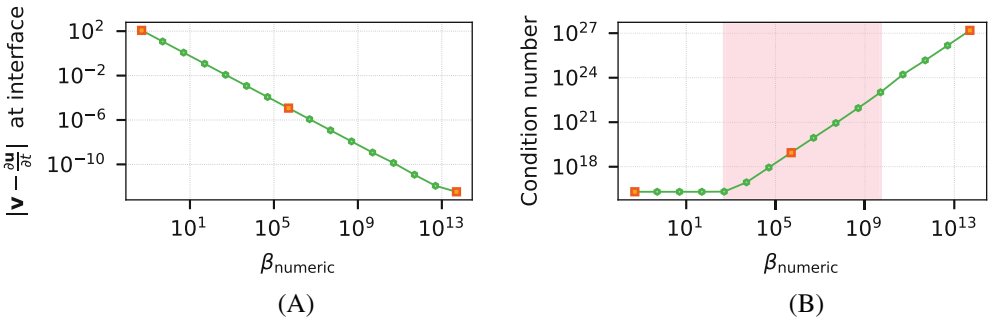

FIGURE 5 Velocity jump and condition number for 1D wave propagation using symmetrization-free formulation. The orange marks show the velocity jump at low $(5 \cdot 10^{-2})$, suitable $(5 \cdot 10^{5})$, and high $(5 \cdot 10^{13})$ numerical penalty factors. The corresponding field solutions are shown in Figure 4. (A) Velocity jump $\left|\boldsymbol{v} - \frac{\partial \boldsymbol{u}}{\partial t}\right|$ at interface versus numerical penalty factor; (B) condition number of the system matrix versus numerical penalty factor

excitation boundary Γ_e. We impose the boundary conditions $v_x = 0\,\text{m/s}$ on Γ_x and $v_y = 0\,\text{m/s}$ on Γ_y. A plot of the resulting velocity vector field is displayed in Figure 6B.

Our second test case aims to study compression waves traveling over the interface. Using the same geometry topology as the previous example (Figure 6A), with different dimensions, we create cylindrical compression waves by harmonic pressure excitation $p = 1\,\text{Pa}$ along boundary Γ_e. The symmetry boundary conditions $(v_n = 0)$ are applied at the symmetry lines Γ_y and Γ_x. Figure 6B shows the velocity vector field of the resulted compression waves. Additionally, to perform the finite element simulation, we consider 364,000, 121,850, and 121,000 DOF for velocity, pressure, and displacement, respectively.

The five material combinations, with a wide range of density ratios varying from $0.15 \cdot 10^{-3}$ to 0.89, are considered to examine the robustness of the penalty factor. These combinations include air-steel, air-rubber, water-steel, water-nylon, and water-foam. The properties of the fluid and solid materials are described in Table 1.

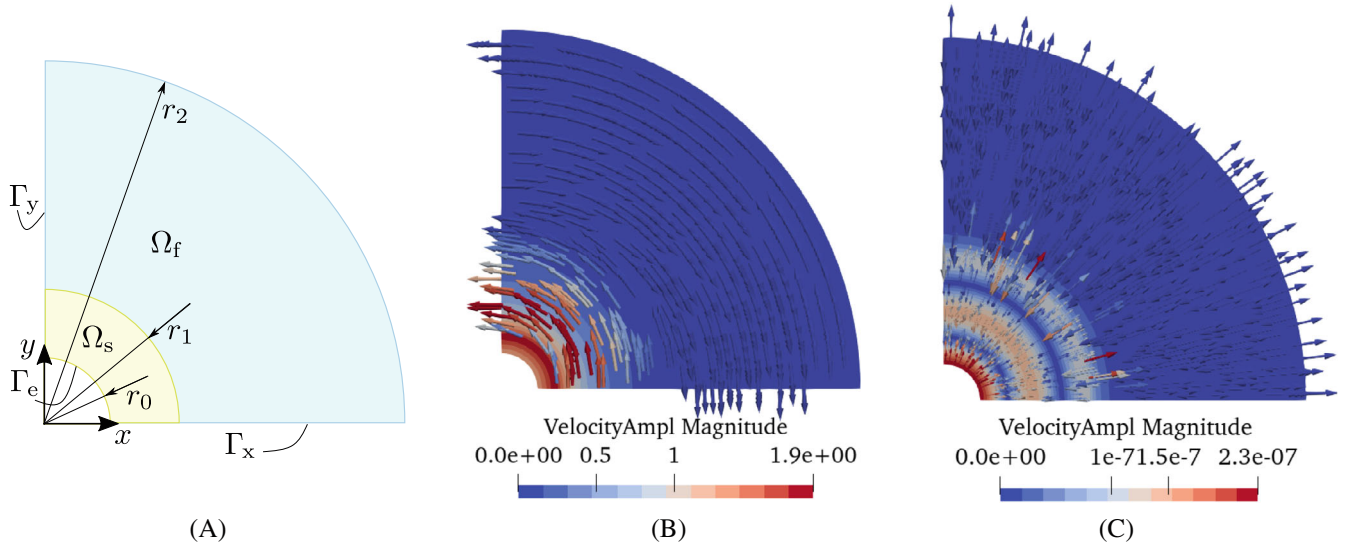

FIGURE 6 (A) Disc sketch and velocity field results. (A) Schematics of the disc considered for simulations. Blue color depicts the fluid region (Ω_f) and yellow color depicts the solid region (Ω_s); (B) Simulated velocity field for the rotating disc example for air-steel material combination (m/s); (C) Simulated velocity field for the cylindrical wave example for air-steel material combination (m/s)

TABLE 2 Test cases dimensions

	Cylindrical wave			Rotating disc		
	r_1 (m)	r_2 (m)	f (MHz)	r_1 (m)	r_2 (m)	f (kHz)
Air-steel	$8.0 \cdot 10^{-5}$	$20.0 \cdot 10^{-5}$	60	$3.0 \cdot 10^{-5}$	$20.0 \cdot 10^{-5}$	10
Air-rubber	$3.0 \cdot 10^{-5}$	$300.0 \cdot 10^{-5}$	10	$3.0 \cdot 10^{-5}$	$20.0 \cdot 10^{-5}$	10
Water-steel	$5.0 \cdot 10^{-5}$	$350.0 \cdot 10^{-5}$	260	$3.0 \cdot 10^{-5}$	$20.0 \cdot 10^{-5}$	1
Water-nylon	$3.0 \cdot 10^{-5}$	$351.0 \cdot 10^{-5}$	230	$3.0 \cdot 10^{-5}$	$20.0 \cdot 10^{-5}$	1
Water-foam	$3.0 \cdot 10^{-5}$	$351.0 \cdot 10^{-5}$	230	$3.0 \cdot 10^{-5}$	$20.0 \cdot 10^{-5}$	1

For a realistic comparison among the simulations with different materials, we design the test cases such that only a traveling wave field is encountered in the fluid region. This is accomplished by adapting the fluid region and the excitation frequency such that the wave amplitudes have decayed sufficiently until the outer boundary is reached, thereby avoiding reflections. To do so, we consider different material combinations for different dimensions and frequencies. Table 2 describes the dimensions and the frequencies for each of these examples.

Figure 6B,C also show the velocity field results of the simulation for air-steel material combination for rotating and cylindrical discs, respectively. These figures depict a continuous velocity field at the fluid–solid interface, indicating that our formulation was successfully applied on curved interfaces. We note that the velocity fields were radially symmetric in both examples as a result of the rotationally symmetric excitation applied to the disc at Γ_e (Figure 6A).

4.2.1 | Choice of penalty factor and formulation

To obtain the suitable ranges of the numerical penalty factor in symmetrization-free formulation, we examine the velocity error (with a fine mesh as a reference) in response to varied numerical penalty factors for various sets of material combinations in both cylindrical wave and rotating disc examples. As expected, the velocity error for all cases decreases with the rising numerical penalty factor until a plateau is reached when the numerical penalty factor is sufficiently high. The expected increase in velocity error for too large numerical penalty factors is often not visible in the plots since the solver cannot solve the system matrix due to its ill-conditioning. The suitable numerical penalty factor is the range where the test cases have low errors for all the material combinations. Figure 7A,B

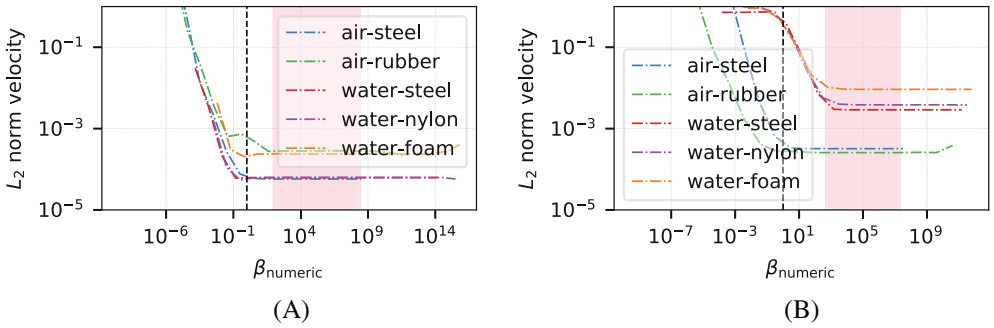

FIGURE 7 Velocity error obtained for a range of numerical penalty factors with various material combinations for both test cases in the symmetrization-free formulation. Pink regions show the suitable range of numerical penalty factors where the error is minimum for all the scenarios. Dashed lines (- - -) mark $\beta = \beta_{\text{scaling}}$ (i.e., $\beta_{\text{numeric}} = 1$). (A) Rotating disc: symmetrization-free formulation; (B) cylindrical wave: symmetrization-free formulation

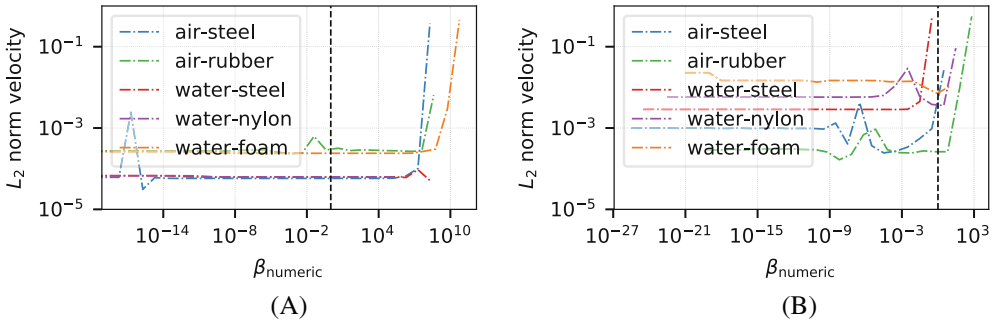

FIGURE 8 Velocity error as in Figure 7 but for the Nitsche-based formulation. (A) Rotating disc: Nitsche-based formulation with symmetrization term; (B) Cylindrical wave: Nitsche-based formulation with symmetrization term

show that the suitable ranges of numerical penalty factor for the rotating disc ($10^2 - 2 \cdot 10^8$) and cylindrical disc ($5 \cdot 10^2 - 2 \cdot 10^7$) examples are reasonably large. The black dashed lines marked in these figures indicate the errors for the $\beta_{\text{numeric}} = 1$. This value of the numerical penalty factor does not generate the optimal results. In general, considering the 1D wave propagation, the numeric penalty factor between $5 \cdot 10^2 - 2 \cdot 10^7$ is suggested. This numerical penalty factor scales the penalty bi-linear terms 3–7 orders of magnitude higher than the other bi-linear terms.

The Nitsche-based formulation retains the symmetrization term in Equation (13). Here we compare the numerical results with and without this symmetrization term in the rotating disc and cylindrical wave examples. Figure 8 shows that low errors are obtained with a wide range of numerical penalty factors using the Nitsche-based formulation. In comparison to the symmetrization-free formulation (Figure 7) the values of the numerical penalty factor are lower; however, both formulations use different expressions for β_{scaling} (compare Equations (24) and (25)). Similar to 1D wave propagation, the errors remain low for very low values of the penalty factor. This indicates that the symmetrization term alone without including the jump term is sufficient to satisfy the coupling condition. Unlike the 1D wave propagation, $\beta_{\text{numeric}} = 1$ does not suggest the lowest error in the cylindrical wave propagation.

The Nitsche-based formulation uses more numerical effort than the symmetrization-free formulation, since the additional symmetrization term needs to be assembled. Given the correct penalty factors, the numerical errors of both formulations are comparable and deliver equivalent results (Figures 7 and 8). For instance, identical results of the simulated velocity fields by two approaches are shown in Figure 9, using the air-steel material combination in rotating disc example. The velocity continuity is fulfilled at the solid–fluid interfaces, and the velocity decays in the fluid field due to the shear viscosity effect. For these two simulations suitable numerical penalty factors of 10^{-4} and 10^4 were used for the Nitsche-based and symmetrization-free formulations, respectively.

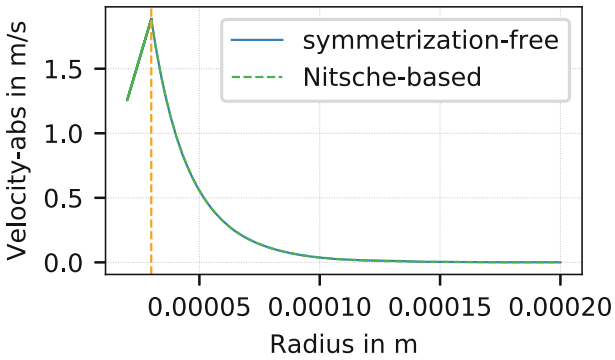

FIGURE 9 Velocity field results in diameter line in rotating disc example

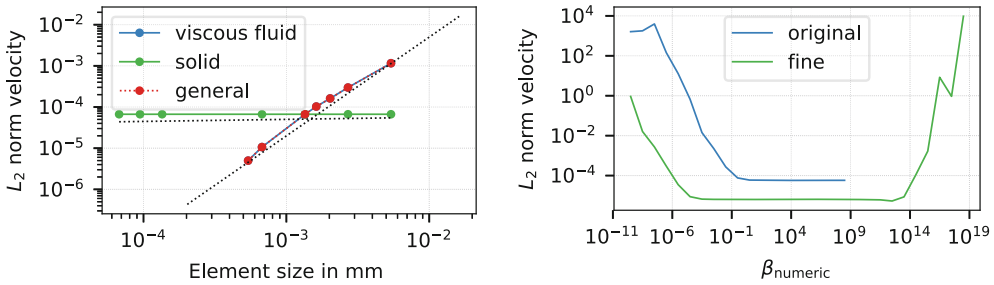

FIGURE 10 Mesh study in rotating disc example. (A) L_2 relative error in velocity versus element size h when the mesh is refined in the viscous fluid domain (blue), solid domain (green), and generally in both domains (red). The dashed black lines indicate the convergence rates ($E = ch^n$); (B) L_2 relative error norm (E) in velocity versus numerical penalty factor at two different mesh discretizations. Original mesh (used in previous error study) and the finer mesh have $\sim 1.2 \cdot 10^4$ and $\sim 10^5$ DOF, respectively.

4.2.2 | Numerical convergence

Having a non-conforming fluid–solid interface gives us the opportunity to independently refine the mesh in solid or/and fluid domains. To study the spatial convergence, we choose the rotating disc example with air-steel material and uniformly refine the mesh in both domains simultaneously and in each domain separately. The study is performed using the symmetrization-free formulation, instead of mathematical proof for convergence. Figure 10A shows the relative L_2 error versus the element size h, employing a numerical penalty factor of 10^6. These relative errors (of the fluid velocity field) are evaluated with respect to the case of the finest mesh with solid and fluid element size of $\sim 4 \cdot 10^{-5}$ and $\sim 4 \cdot 10^{-4}$ mm, respectively. The error is expected to behave like $E = ch^n$, where n denotes the order of convergence and c is an arbitrary positive constant. Our results show a convergence order of (approximately) 2.4 for both uniform and fluid refinement ($n \sim 2.4$) and very low convergence for the refinement of the solid domain alone. The error reduction in the solid domain is much lower than the viscous flow and is relatively constant.

We further discuss the effect of the numerical penalty factors on the velocity error concerning the mesh discretizations in Figure 10B. This figure shows that for the case of the finer mesh with 10^5 DOF, not only the system creates one order of magnitude lower errors, but also the plateau of the minimum error is larger than the original mesh (which was used in Section 4.2.1). In the original case, the large condition number of the system matrix for the numerical penalty factor higher than $5 \cdot 10^8$ prevents our solver from achieving further results. Therefore, the suitable range of the numerical penalty factor is 10-$5 \cdot 10^8$. However, for the finer mesh a larger range of the numerical penalty factor (10^{-4}-$5 \cdot 10^{12}$) is possible.

4.3 | Helmholtz resonator with flexible end-plate

Helmholtz resonators are used in multiple industrial applications, including monitoring pollution,[43] suppressing engine noise,[44] and attenuating flow pulsation in the hydraulic and acoustic systems.[45,46] Helmholtz resonator attenuates the

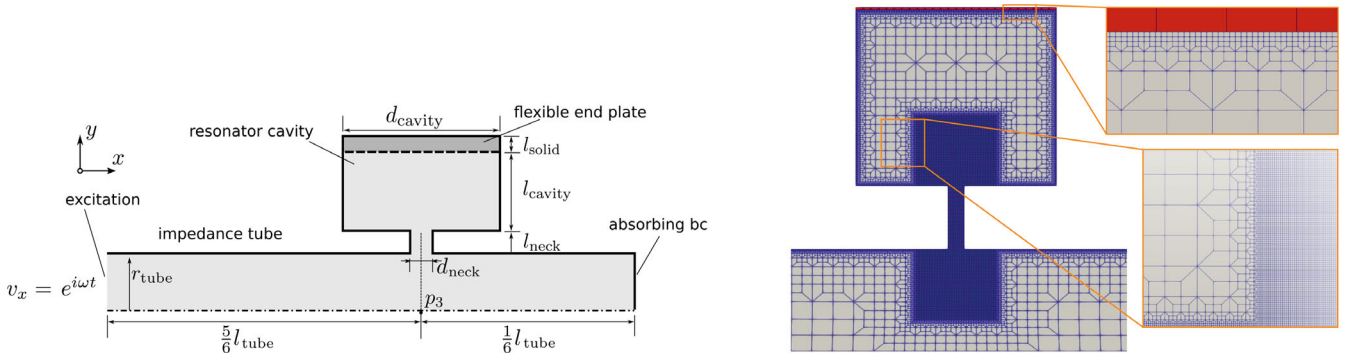

FIGURE 11 Helmholtz resonator sketch, boundary conditions, and mesh discretization. (A) Problem sketch and boundary conditions; (B) Helmholtz resonator mesh discretization. Finer mesh are considered near walls and in neck where the viscous boundary layers exist

TABLE 3 Helmholtz resonator geometry parameters and solid material

l_{tube}(mm)	r_{tube}(mm)	l_{neck}(mm)	d_{neck}(mm)	l_{cavity}(mm)	d_{cavity}(mm)	l_{solid}(mm)	ρ(kg/m^3)	ν	E(Pa)
400	14.5	9	2	25	25	0.39	320	0.383	35.3 e^6

acoustic energy over a certain frequency band that corresponds to its resonant frequencies. Two common approaches used for tuning the resonant frequencies are incorporating multiple Helmholtz resonators in parallel and series,[45,47] and using a flexible plate at the end of Helmholtz cavity.[48-51] The former, however, is not applicable in miniature designs because it requires more space. Thus, in the current study, we use our method for modeling the fluid-structure interaction to design a miniature Helmholtz resonator with a flexible end-plate, applicable in small volume spaces. This approach provides flexible applications for obtaining one or multiple resonance frequencies, tuned with those of the plate depending on the plate geometry and its material properties.

The geometry and dimensions of our Helmholtz resonator test case and arbitrary solid material properties are provided in Figure 11A and Table 3, respectively. As shown in Figure 11A in a Helmholtz resonator, an impedance tube is attached to a cavity through a neck. The absorbing boundary condition is considered at the end of the impedance tube to simulate free-field conditions. For viscous acoustics, this condition is

$$\boldsymbol{\sigma}_{\mathrm{f}} = z_0(\boldsymbol{v}\cdot\boldsymbol{n})\boldsymbol{n}, \tag{28}$$

where $z_0 = \rho c$ is the specific impedance. We apply the normal harmonic velocity $\boldsymbol{v}_x = 1$ on the excitation boundary. In addition, we consider wall on the other fluid boundaries and fix the flexible plate on its two sides (clamped plate). Thanks to symmetric geometry, we model half of the Helmholtz resonator and apply symmetry conditions on the bottom boundary (dashed line in Figure 11A). Due to the Helmholtz resonator's small dimension and long narrow neck, viscose effects are relevant.[46] While in the cavity and impedance tube the mesh size is 2.36 mm, due to the relevance of the viscous effect in the neck and in viscous boundary layers close to walls, a finer mesh size (17.4 μm) is applied. The mesh size in the solid region is 0.21 mm, creating the non-conforming mesh discretization at the solid–fluid interface. Figure 11B shows the mesh discretizations. Furthermore, air and arbitrary solid material properties used in the current study are provided in Tables 1 and 3, respectively.

To investigate the impact of solid interaction on system resonance frequencies, a comparison is made between the Helmholtz resonator's resonance frequencies with flexible end-plate (modified hereafter) and without flexible end-plate (unmodified hereafter). Furthermore, to demonstrate the viscous effect, the results are compared to those from the standard wave equation. The other conditions, including material and dimension, remain the same. Since the resonance frequencies are pronounced in the transmission loss (TL), we study it over a certain frequency range (1–1200 Hz). The transmission loss is

$$TL = 20\log\left(\frac{1}{T}\right), \tag{29}$$

where T is the transmission coefficient. This coefficient is defined for an impedance tube by

$$T = \frac{p_3}{p_{\text{in}}}, \tag{30}$$

where p_{in} is the incident pressure. We calculate p_{in} from fitting a 1D wave propagation pattern ($p = p^+e^{-kx} + p^-e^{kx}$) with a complex wave number k (more details are provided in Appendix A) to the upstream flow. In doing so, p_{in} computes by

$$p_{\text{in}} = p^+ e^{-kx}{}_{x=\frac{5}{6}l_{\text{tube}}}. \tag{31}$$

The transmission loss over frequency for modified and unmodified Helmholtz resonator for viscous and inviscid flow is displayed in Figure 12. This figure shows, for viscous flow, the unmodified Helmholtz resonator has a resonance frequency of 850 Hz compared to the two resonance frequencies of the modified Helmholtz resonator observed at 151 and 1061 Hz. Therefore, by employing the modified Helmholtz resonator, two frequencies in the primary system can be attenuated in comparison to a single frequency of the unmodified Helmholtz resonator. It is evident that the resonance of the modified Helmholtz resonator is lower than the plate's first resonance (235 Hz) and the unmodified Helmholtz resonator's resonance frequency. The second resonance frequency of the modified Helmholtz resonator is between the unmodified Helmholtz resonator (850 Hz) and the third resonant frequency of the plate (1266 Hz). It is worthy of note that the second plate resonance frequency is not excited due to an asymmetric shape mode.

Interestingly, consistent with the two resonance frequencies of the modified Helmholtz resonator, the plate in the modified resonator also shows its first and third resonance frequency mode shape behaviors at 151 and 1061 Hz. The solid displacement behaviors at these frequencies are shown in Figure 13. Solid displacement behavior at the modified Helmholtz resonator resonance frequencies causes variations in the fluid velocity field. In the first resonant frequency, the fluid moves toward both middle of the cavity and plate where the solid has the higher displacement amplitude (Figure 13A). Whereas, in the second resonant frequency the direction of fluid is toward the sides of the cavity and going further away from the middle of the cavity, corresponding to the plate deformation (Figure 13B).

The inviscid flow shows higher resonance frequencies than the viscous flow (Figure 12). The differences in the resonance frequencies are more pronounced in the modified Helmholtz resonator where the first resonance frequency of the inviscid flow is 129 Hz higher than that in the viscous flow. This result demonstrates that the viscous dissipation significantly impacts the resonance frequencies of the Helmholtz resonator and cannot be ignored. Moreover, the peak values of the transmission loss in inviscid flow is larger than that in the viscous flow announcing the viscous damping effects.

Finally, we study the transmission, reflection and the absorption energy coefficients in modified and unmodified Helmholtz resonators in the cases with viscous effect, and without the viscous effects. From the law of conservation of energy the energy absorption coefficient (A) is defined as[52]

$$A = 1 - R^2 - T^2, \tag{32}$$

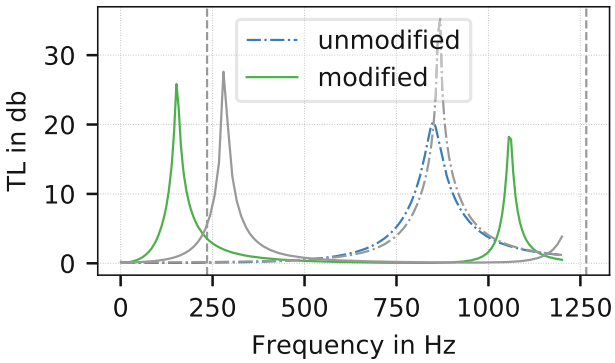

FIGURE 12 Transmission loss of the unmodified and modified Helmholtz resonator for viscous and inviscid (gray results) flow. The gray dashed lines (- - -) show first and third mechanical resonance frequencies.

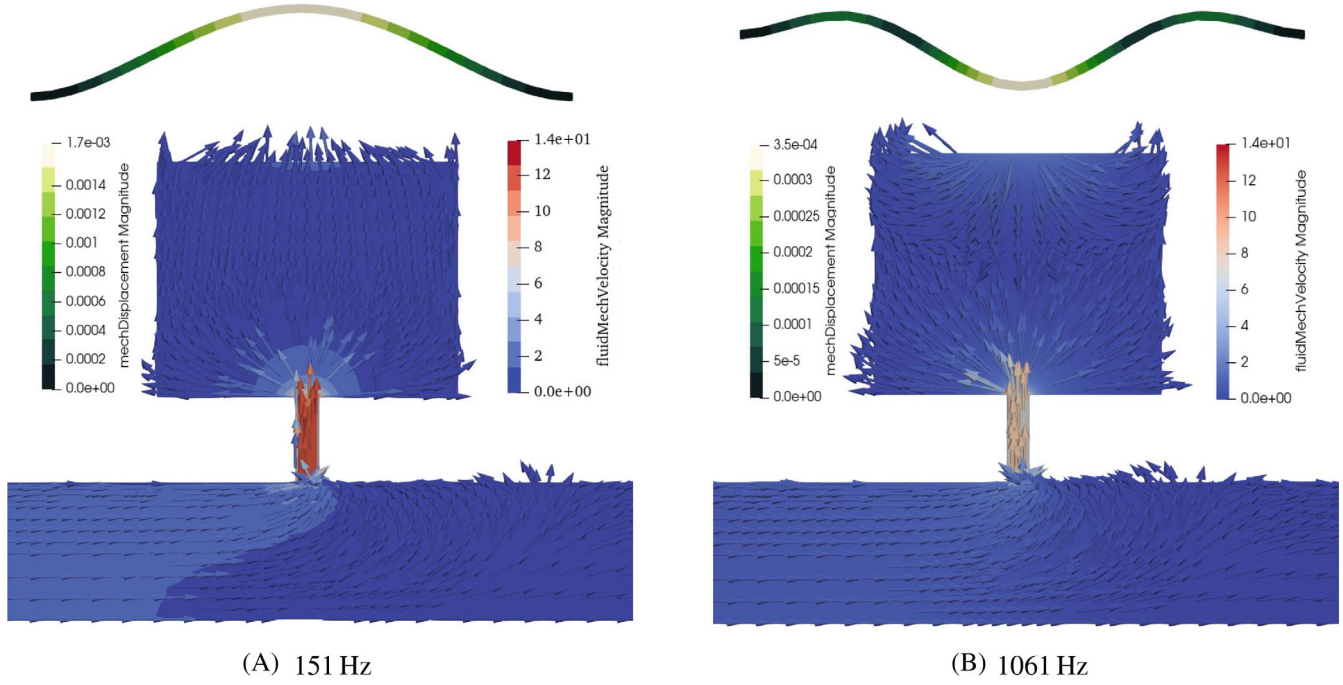

FIGURE 13 Plate shape mode at the resonance frequencies of the modified Helmholtz resonator ((A) 151 Hz and (B) 1061 Hz). Plate exhibit its first and third mode shapes.

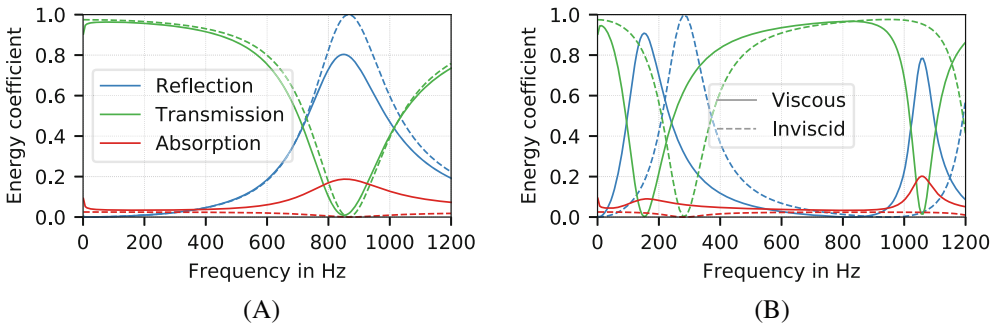

FIGURE 14 Reflection, transmission, and absorption energy coefficients (blue, green, red) in the viscous (solid lines) and in the inviscid (dashed lines) flows in unmodified (without solid plate), and modified (with solid plate) Helmholtz resonator. (A) Unmodified Helmhltz resonator; (B) modified Helmhltz resonator

where the reflection coefficient (R) computes by

$$R = \frac{p^{-}e^{kx}}{p^{+}e^{-kx}}. \tag{33}$$

Figure 14 displays the reflection, transmission and absorption energy coefficients versus frequency in the unmodified (Figure 14A) and modified (Figure 14B) Helmholtz resonators. The energy coefficients of reflection and transmission are the square of those coefficients (R^2 and T^2, respectively). In the modified Helmholtz resonator, unlike the unmodified one, the absorption and the reflection energy coefficients, each, have two peaks that correspond to the two observed resonance frequencies. In the viscous flow, the amplitude of the energy absorption coefficient in the second resonance is ~10% higher than the one in the unmodified resonance; however, in the first resonance, which results from plate resonance, has a lower absorption coefficient. The inviscid flow has zero transmission at the resonance frequencies (see Figure 14). Since no absorption is possible without viscous effects ($A = 0$), this means that all the waves are reflected ($R = 1$). In contrast, the viscous flow has significant absorption at the expense of higher transmission coefficients, resulting in lower reflection.

5 | CONCLUSIONS

In this contribution, we presented a non-conforming finite element approach for solving FSI problems, which allows an optimal mesh size for each physical field. The full linearized Navier–Stokes equations and balance of momentum were used to model a viscous compressible fluid and an elastic solid, respectively. Furthermore, we proposed an estimation for the penalty factor using the scaling approach. The FEM formulation can be implemented in a Nitsche-based and a symmetrization-free variant, which were validated and compared by four case studies.

In the first case study, we analyzed the effect of low, suitable, and high numerical penalty factors on the errors, field results, and velocity jump in the symmetrization-free formulation. Compared to the analytical solution, the suitable range of the numerical penalty factor had a precision of 10^{-7}. In addition, we showed an inverse relationship between the numerical penalty factor and velocity jump at the interface.

The second and third case studies analyzed the coupling approach, emphasizing the shear and bulk viscosity effects in multiple fluid and solid material combinations in both formulations. Results indicated that numerical penalty factors ranging from $5 \cdot 10^2$ to $2 \cdot 10^7$ (suitable numerical penalty factor) create negligible field errors in the mentioned test cases with the symmetrization-free formulation. The Nitsche-based formulation does not have a limitation on the lower limit of the numerical penalty factor and $\beta_{\text{numeric}} < 10^{-3}$ is considered as a suitable range of numerical penalty factor in this formulation. On the other hand, the assembly effort is lower in the symmetrization-free formulation. Comparison of the Nitsche-based and symmetrization-free formulation in these three cases showed equivalent results while using a suitable penalty factor. In the rotating disc test case, the spatial convergence study showed reasonable convergence rates. Moreover, results revealed that a larger range of numerical penalty factors is valid for finer mesh discretizations.

The last case study investigated the effect of solid interaction on a viscous compressible flow in a miniature Helmholtz resonator by employing our method. This flexible end-plate was added to the resonator to attenuate multiple frequencies. Furthermore, we demonstrated the importance of modeling viscous effects in order to accurately predict the transmission loss and the transmission, absorption, and reflection coefficients. In conclusion, we showed that our formulation has a wide range of applications in modeling FSI in miniature systems.

ACKNOWLEDGMENT

This work was partly funded by the Austrian Research Promotion Agency (FFG) within the program line "Bridge" (project number 868033). The authors acknowledge TU Wien Bibliothek for financial support through its Open Access Funding Programme.

CONFLICT OF INTEREST

The authors declare no potential conflict of interests.

DATA AVAILABILITY STATEMENT

The data that support the findings of this study are available from the corresponding author upon reasonable request.

ORCID

Hamideh Hassanpour Guilvaiee https://orcid.org/0000-0002-8141-0882

REFERENCES

1. Rohan E, Naili S. Homogenization of the fluid–Structure interaction in acoustics of porous media perfused by viscous fluid. *Z Angew Math Phys*. 2020;71(4):1-28. doi:10.1007/s00033-020-01361-1
2. Van Eysden CA, Sader JE. Frequency response of cantilever beams immersed in viscous fluids. *Reson MEMS Princ Model Implem Appl*. 2015;84(1):29-53. doi:10.1002/9783527676330.ch2
3. Van Eysden CA, Sader JE. Frequency response of cantilever beams immersed in compressible fluids with applications to the atomic force microscope. *J Appl Phys*. 2009;106(9):94904. doi:10.1063/1.3254191
4. Bathe KJ, Zhang H. Finite element developments for general fluid flows with structural interactions. *Int J Numer Methods Eng*. 2004;60(1):213-232. doi:10.1002/nme.959
5. Kuhl E, Hulshoff S, de Borst R. An arbitrary Lagrangian Eulerian finite-element approach for fluid-structure interaction phenomena. *Int J Numer Methods Eng*. 2003;57(1):117-142. doi:10.1002/nme.749
6. Dettmer W, Perić D. A computational framework for fluid-rigid body interaction: finite element formulation and applications. *Comput Methods Appl Mech Eng*. 2006;195(13-16):1633-1666. doi:10.1016/j.cma.2005.05.033
7. Kadapa C, Dettmer WG, Perić D. A stabilised immersed boundary method on hierarchical b-spline grids for fluid–Rigid body interaction with solid–Solid contact. *Comput Methods Appl Mech Eng*. 2017;318:242-269. doi:10.1016/j.cma.2017.01.024

8. Nitsche J. Über ein Variationsprinzip zur Lösung von Dirichlet-Problemen bei Verwendung von Teilräumen, die keinen Randbedingungen unterworfen sind. *Abhandlungen aus dem Mathematischen Seminar der Universität Hamburg*. 1971;36(1):9-15. doi:10.1007/BF02995904
9. Liu B. A Nitsche stabilized finite element method: application for heat and mass transfer and fluid–Structure interaction. *Comput Methods Appl Mech Eng*. 2021;386:114101. doi:10.1016/j.cma.2021.114101
10. Hansbo P. Nitsche's method for interface problems in computational mechanics. *GAMM-Mitteilungen*. 2005;28(2):183-206. doi:10.1002/gamm.201490018
11. Ager C, Schott B, Winter M, Wall W. A Nitsche-based cut finite element method for the coupling of incompressible fluid flow with poroelasticity. *Comput Methods Appl Mech Eng*. 2019;351:253-280. doi:10.1016/j.cma.2019.03.015
12. Burman E, Fernández MA, Frei S. A Nitsche-based formulation for fluid-structure interactions with contact. *ESAIM Math Model Numer Anal*. 2020;54(2):531-564. doi:10.1051/m2an/2019072
13. Baaijens FPT. A fictitious domain/mortar element method for fluid-structure interaction. *Int J Numer Methods Fluids*. 2001;35(7):743-761. doi:10.1002/1097-0363(20010415)35:7<743::AID-FLD109>3.0.CO;2-A
14. Boffi D, Cavallini N, Gastaldi L. The finite element immersed boundary method with distributed Lagrange multiplier. *SIAM J Numer Anal*. 2015;53(6):2584-2604. doi:10.1137/140978399
15. Boffi D, Gastaldi L. A fictitious domain approach with Lagrange multiplier for fluid-structure interactions. *Numer Math*. 2017;135(3):711-732. doi:10.1007/s00211-016-0814-1
16. Hansbo P, Hermansson J. Nitsche's method for coupling non-matching meshes in fluid-structure vibration problems. *Comput Mech*. 2003;32(1-2):134-139. doi:10.1007/s00466-003-0467-7
17. Hansbo P, Hermansson J, Svedberg T. Nitsche's method combined with space-time finite elements for ALE fluid-structure interaction problems. *Comput Methods Appl Mech Eng*. 2004;193(39-41 Special Issue):4195-4206. doi:10.1016/j.cma.2003.09.029
18. Loffredo FS, Steinhauser ML, Gannon J, Lee RT. Bone marrow-derived cell therapy stimulates endogenous cardiomyocyte progenitors and promotes cardiac repair. *Cell Stem Cell*. 2011;8(4):389-398. doi:10.1016/j.stem.2011.02.002
19. Burman E, Fernández MA. An unfitted Nitsche method for incompressible fluid–Structure interaction using overlapping meshes. *Comput Methods Appl Mech Eng*. 2014;279:497-514. doi:10.1016/j.cma.2014.07.007
20. Dettmer WG, Kadapa C, Perić D. A stabilised immersed boundary method on hierarchical b-spline grids. *Comput Methods Appl Mech Eng*. 2016;311:415-437. doi:10.1016/j.cma.2016.08.027
21. Veijola T, Turowski M. Compact damping models for laterally moving microstructures with gas-rarefaction effects. *J Microelectromech Syst*. 2001;10(2):263-273. doi:10.1109/84.925777
22. Beltman WM. Viscothermal wave propagation including acousto-elastic interaction, Part I: applications. *J Sound Vib*. 1999;227(3):587-609. doi:10.1006/jsvi.1999.2356
23. Trochidis A. Vibration damping due to air or liquid layers. *Acust*. 1982;51(4):201-212.
24. Bossart R, Joly N, Bruneau M. Hybrid numerical and analytical solutions for acoustic boundary problems in thermo-viscous fluids. *J Sound Vib*. 2003;263(1):69-84. doi:10.1016/s0022-460x(02)01098-2
25. Berggren M, Bernland A, Noreland D. Acoustic boundary layers as boundary conditions. *J Comput Phys*. 2018;371:633-650. doi:10.1016/j.jcp.2018.06.005
26. Beltman WM. Viscothermal wave propagation including acousto-elastic interaction, part I: theory. *J Sound Vib*. 1999;227(3):555-586.
27. Beltman WM. *Viscothermal Wave Propagation Including Acousto-Elastic Interaction*. PhD thesis. University of Twente; 1998.
28. Nijhof MJJ. *Viscothermal Wave Propagation*. PhD thesis. Universiteit Twente; 2010.
29. Kampinga WR, Wijnant YH, de Boer A. An efficient finite element model for viscothermal acoustics. *Acta Acust Unit Acust*. 2011;97(4):618-631. doi:10.3813/AAA.918442
30. Kampinga WR, Wijnant YH, de Boer A. Performance of several viscothermal acoustic finite elements. *Acta Acust Unit Acust*. 2010;96(1):115-124. doi:10.3813/aaa.918262
31. Kaltenbacher M, Toth F, Hassanpour H. openCFS. https://opencfs.org.
32. Gunzburger M. *Finite Element Methods for Viscous Incompressible Flows*. Academic Press, 1986.
33. Fortin M. Finite element solution of the Navier-Stokes equations. *Acta Numer*. 1993;2:239-284. doi:10.1017/S0962492900002373
34. Fritz A, Hüeber S, Wohlmuth BI. A comparison of mortar and Nitsche techniques for linear elasticity. *Calcolo*. 2004;41(3):115-137. doi:10.1007/s10092-004-0087-4
35. Kaltenbacher M. *Numerical Simulation of Mechatronic Sensors and Actuators*. Springer; 2015.
36. Hansbo A, Hansbo P. An unfitted finite element method, based on Nitsche's method, for elliptic interface problems; 2016:16. doi:10.1016/S0045-7825(02)00524-8
37. Flemish B. *Non-matching Triangulations of Curvilinear Interfaces Applied to Electro-Mechanics and Elasto-Acoustics*. PhD thesis. University of Stuttgart; 2006.
38. Kaltenbacher M, Floss S. Nonconforming finite elements based on nitsche-type mortaring for inhomogeneous wave equation. *J Theor Comput Acoust*. 2018;26(3):1-18. doi:10.1142/S2591728518500287
39. Jiang W, Annavarapu C, Dolbow JE, Harari I. A robust Nitsche's formulation for interface problems with spline-based finite elements. *Int J Numer Methods Eng*. 2015;104(February):676-696. doi:10.1002/nme.4766
40. Schenk O, Gärtner K. *Pardiso*. Springer; 2011:1458-1464.
41. Developer Reference for Intel® oneAPI math kernel library - C.
42. Henríquez VC, Andersen PR, Jensen JS, Juhl PM, Sánchez-Dehesa J. A numerical model of an acoustic metamaterial using the boundary element method including viscous and thermal losses. *J Comput Acoust*. 2017;25(4):1750006. doi:10.1142/S0218396X17500060

43. Zeninari V, Kapitanov VA, Courtois D, Ponomarev YN. Design and characteristics of a differential Helmholtz resonant photoacoustic cell for infrared gas detection. *Infrared Phys Technol*. 1999;40(1):1-23. doi:10.1016/S1350-4495(98)00038-3
44. Liu F, Phipps A, Horowitz S, et al. Acoustic energy harvesting using an electromechanical Helmholtz resonator. *J Acoust Soc Am*. 2008;123(4):1983-1990. doi:10.1121/1.2839000
45. Guan C, Jiao Z. Modeling and optimal design of 3 degrees of freedom Helmholtz resonator in hydraulic system. *Chin J Aeronaut*. 2012;25(5):776-783. doi:10.1016/S1000-9361(11)60444-5
46. Komkin AI, Mironov MA, Bykov AI. Sound absorption by a Helmholtz resonator. *Acoust Phys*. 2017;63(4):385-392. doi:10.1134/S1063771017030071
47. Han Y, Lv H. Research on muffler performance control by arrangement of Helmholtz resonators. Proceedings of the 2015 3rd International Conference on Machinery, Materials and Information Technology Applications; Vol. 1, Icmmita:1307-1310. doi:10.2991/icmmita-15.2015.242
48. Nudehi SS, Duncan GS, Farooq U. Modeling and experimental investigation of a Helmholtz resonator with a flexible plate. *J Vibr Acoust Trans ASME*. 2013;135(4):1-6. doi:10.1115/1.4023810
49. Sanada A, Tanaka N. Extension of the frequency range of resonant sound absorbers using two-degree-of-freedom Helmholtz-based resonators with a flexible panel. *Appl Acoust*. 2013;74(4):509-516. doi:10.1016/j.apacoust.2012.09.012
50. Kurdi MH, Duncan GS, Nudehi SS. Optimal design of a Helmholtz resonator with a flexible end plate. *J Vibr Acoust Trans ASME*. 2014;136(3):1-8. doi:10.1115/1.4026849
51. Cui S, Harne RL. Acoustic-structure interaction in an adaptive Helmholtz resonator by compliance and constraint. *J Vibr Acoust Trans ASME*. 2020;142(2):1-10. doi:10.1115/1.4045456
52. Antonets IV, Kotov LN, Shavrov VG, Shcheglov VI. Reflection, transmission, and absorption coefficients calculated for the oblique incidence of an electromagnetic wave on a plate. *J Commun Technol Electron*. 2008;53(4):363-376. doi:10.1134/S1064226908040013

How to cite this article: Hassanpour Guilvaiee H, Toth F, Kaltenbacher M. A non-conforming finite element formulation for modeling compressible viscous fluid and flexible solid interaction. *Int J Numer Methods Eng*. 2022;123(24):6127-6147. doi: 10.1002/nme.7106

APPENDIX A. ANALYTICAL SOLUTION FOR 1D WAVE PROPAGATION

Here, we aim to obtain an analytical solution for 1D wave propagation in a viscous compressible fluid coupled to solid mechanics. We start with the balance of momentum for the solid for a linear elastic material behavior without body forces

$$\rho_s \frac{\partial^2 \boldsymbol{u}}{\partial t^2} - \nabla \cdot \left(C : \frac{1}{2} \left(\boldsymbol{\nabla u} + (\boldsymbol{\nabla u})^T \right) \right) = 0, \tag{A1}$$

where C is the stiffness tensor. In the simplified case of 1D wave propagation, the displacement $\boldsymbol{u}$ can be written as

$$\boldsymbol{u} = (u_x(t,x), 0, 0). \tag{A2}$$

Inserting the displacement formulation (A2) into the momentum conservation (A1) results in

$$\rho_s \frac{\partial^2 u_x}{\partial t^2} - C_{11} \frac{\partial^2 u_x}{\partial x^2} = 0, \tag{A3}$$

where $C_{11} = \frac{E(1-\nu)}{(1+\nu)(1-2\nu)}$, E and ν are Young modulus and Poisson ratio, respectively. The displacement distribution in the channel with symmetry boundary conditions on the top and at the bottom is

$$u_x = e^{i\omega t}(u^+ e^{-k_1 x} + u^- e^{k_1 x}), \tag{A4}$$

with the wavenumber k_1. This wavenumber can be derived by inserting the displacement distribution (A4) into the balance of momentum (A3)

$$k_1 = \pm i \sqrt{\frac{\rho_s \omega^2}{C_{11}}}. \tag{A5}$$

In the case of 1D wave propagation in a compressible viscous fluid, along the x axis, the velocity vector will only have the x component and the pressure is a function of x and time t

$$\boldsymbol{v} = (v_x(x,t), 0, 0) \qquad p = p(x,t).$$

In the adiabatic case, the balance of mass and momentum in 1D wave propagation are

$$\frac{1}{c^2}\frac{\partial p}{\partial t} + \rho\frac{\partial v_x}{\partial x} = 0, \tag{A6}$$

$$\rho\frac{\partial v_x}{\partial t} + \frac{\partial p}{\partial x} - \left(\frac{4}{3}\mu + \mu_b\right)\frac{\partial^2 v_x}{\partial x^2} - \mu\frac{\partial^2 v_x}{\partial y^2} = 0. \tag{A7}$$

By applying the space derivative on the balance of mass and the time derivative on the balance of momentum, we can eliminate the pressure DOF

$$\frac{\partial^2 p}{\partial x \partial t} = -\rho c^2\frac{\partial^2 v_x}{\partial x^2}, \tag{A8}$$

$$\frac{\partial^2 v_x}{\partial t^2} + \frac{\partial^2 p}{\partial x \partial t} - \left(\frac{4}{3}\mu + \mu_b\right)\frac{\partial^3 v_x}{\partial x^2 \partial t} - \mu\frac{\partial^3 v_x}{\partial y^2 \partial t} = 0. \tag{A9}$$

By inserting (A8) into (A9) the linearized momentum equation is

$$\frac{\partial^2 v_x}{\partial t^2} - \rho c^2\frac{\partial^2 v_x}{\partial x^2} - \left(\frac{4}{3}\mu + \mu_b\right)\frac{\partial^3 v_x}{\partial x^2 \partial t} - \mu\frac{\partial^3 v_x}{\partial y^2 \partial t} = 0. \tag{A10}$$

We also know in the simple channel with symmetry boundary conditions on the top and at the bottom, the velocity distribution can be presented as

$$v_x = e^{i\omega t}(v^+ e^{-k_2 x} + v^- e^{k_2 x}), \tag{A11}$$

where, in the case of the attenuation, k_2 is the fluid complex wave number. Applying velocity distribution (A11) in 1D velocity wave propagation (A10) results in

$$-\omega^2\rho v_x - \rho c^2 k_2^2 v_x - \left(\frac{4}{3}\mu + \mu_b\right) i\omega k_2 v_x = 0. \tag{A12}$$

Finally, k_2 will be obtained

$$k_2 = \pm i\sqrt{\frac{\rho\omega^2}{\rho c^2 + \left(\frac{4}{3}\mu + \mu_b\right) i\omega}}. \tag{A13}$$

To obtain the analytical solution, we need four equations to compute the velocity (A11) and displacement (A4) distribution in fluid and solid domains. These four equations are two interface constraints equations and two boundary conditions. The interface constraints were previously mentioned (see (8) and (9)). Starting from continuity of velocity, Equation (9) at the interface, and inserting the displacement (A4) and velocity (A11) distribution yields

$$i\omega(u^+ e^{-k_1 L_1} + u^- e^{k_1 L_1}) = v^+ e^{-k_2 L_1} + v^- e^{k_2 L_1}, \tag{A14}$$

where L_1 is the x-position of the interface. The continuity of traction at the interface for the 1D wave propagation (8) is

$$C_{11}\frac{\partial u_x}{\partial x}\bigg|_{x=L_1} = -p + \left(\mu_b + \frac{4}{3}\mu\right)\frac{\partial v_x}{\partial x}\bigg|_{x=L_1}. \tag{A15}$$

$$\left(c^2\rho_f k_2 + \left(\mu_b + \frac{4}{3}\mu\right) i\omega k_2\right)(v^- e^{k_2 L_1} - v^+ e^{-k_2 L_1}) = C_{11} i\omega k_1 (u^- e^{k_1 L_1} - u^+ e^{-k_1 L_1}), \tag{A16}$$

with the speed of sound c. By adding the boundary conditions, we would be able to obtain all four unknowns.

Figure 2 demonstrates the boundary conditions we considered for the analytical results. The harmonic displacement $u|_{x=0} = 1$ m and the velocity in x direction, at the end of channel ($x = L_1 + L_2$) is considered zero ($v_x|_{x=L1+L_2} = 0$). We derive the boundary condition's equations by inserting the displacement excitation at $x = 0$ into displacement distribution (A4) and velocity variation at $x = L1 + L2$ into the velocity distribution (A11)

$$u^+ + u^- = 1, \tag{A17}$$

$$v^+ e^{-k_2(L_1+L_2)} + v^- e^{k_2(L_1+L_2)} = 0. \tag{A18}$$

The unknowns u^+, u^-, v^+, and v^- will be now derived by solving the set of linear equations (A14), (A16), (A17), and (A18).